Hindawi
Advances in Meteorology
Volume 2024, Article ID 1481661, 15 pages
https://doi.org/10.1155/2024/1481661

Research Article

Diurnal Variation Characteristics of Raindrop Size Distribution Observed by a Parsivel^2 Disdrometer in the Ili River Valley

Yufei Jiang,[1,2,3] **Lianmei Yang**,[1,2,3] **Jiangang Li**,[1,2,3] **Yong Zeng**,[1,2,3] **Zepeng Tong**,[1,2,3] **Xiaomeng Li**,[1,2,3] **and Haoyang Li**[1,2,3]

[1]*Institute of Desert Meteorology, China Meteorological Administration, Urumqi 830002, China*
[2]*Field Scientific Observation Base of Cloud Precipitation Physics in West Tianshan Mountains, Urumqi 830002, China*
[3]*Xinjiang Cloud Precipitation Physics and Cloud Water Resources Development Laboratory, Urumqi 830002, China*

Correspondence should be addressed to Lianmei Yang; yanglm@idm.cn

Received 5 July 2023; Revised 21 December 2023; Accepted 4 January 2024; Published 16 January 2024

Academic Editor: Gabriele Buttafuoco

The diurnal variation characteristics of raindrop size distribution (RSD) in the Ili River Valley are investigated in this study, using the RSD data from May to September during 2020-2021 collected by a Parsivel^2 disdrometer in Zhaosu. Significant diurnal variations (02–07, 08–13, 14–19, and 20-01 local standard time (LST)) of precipitation and RSD in Zhaosu are revealed during the rainy seasons. Precipitation mainly occurs in the late afternoon and early evening. A higher concentration of small raindrops is observed in the morning, whereas more mid-size and large raindrops are observed in the afternoon. The RSD exhibits diurnal differences between different rainfall rate classes; the diurnal difference of RSD is more pronounced in the case of high rainfall rates. Stratiform precipitation can occur at any time of the day, yet convective precipitation mainly occurs during the late afternoon and early evening. The RSD of stratiform rainfall shows a similar distribution over the four time periods. For convective rainfall, the concentration of small raindrops is the highest (lowest) over 02–07 (14–19) LST, while the highest (lowest) concentration of medium and large drops is observed over 14–19 (02–07) LST. Convective rain in the Ili River Valley over 14–19 LST can be characterized as the continental convective cluster, while in the rest time of the day, it is neither in the maritime cluster nor in the continental cluster. The empirical relationships between the radar reflectivity factor and rainfall rate (Z-R) for stratiform and convective rain types are also derived. The purpose of this study is to advance our understanding of precipitation microphysics in arid mountainous region.

1. Introduction

Raindrop size distribution (RSD) reflects the distribution of the number of raindrops per unit volume with raindrop diameter, which is an important way to better understand the microphysical characteristics of clouds and precipitation [1–6]. Spatial and temporal variations of RSD are closely related to a series of microphysical processes, such as nucleation, vapour growth, collision and coalescence, riming, breakup, and melting [7–9]. Understanding the variability of RSD is of great importance for improving radar quantitative precipitation estimation (QPE) [10–13], optimizing microphysical parameterization schemes in numerical weather and climate models [14–16] and assessing the effect of weather modification [17]. In addition, RSD plays an important role in the studies of runoff process, flood control, disaster mitigation, and soil erosion [18–21].

Many studies have shown that there are obvious temporal and spatial variations in RSD characteristics in terms of rainfall rate and type due to differences in climate background, geographical location, and atmospheric condition [22–29]. Based on observations of two different disdrometers and radar retrievals, Bringi et al. [1] analyzed RSD characteristics under various climate regimes and found that there are significant sea-land dissimilarities in convective rainfall. The continental-like cluster is characterized by a higher mass-weighted mean diameter, while the maritime-like cluster is characterized by a lower mass-weighted mean diameter. Dolan et al. [30] employed principal component analysis (PCA) to reveal comprehensive modes of spatial and temporal variations of RSD spanning from the deep tropics to the high latitudes. They conceived that the physical processes responsible for shaping the RSD appear to vary as a function of latitude. Marzuki et al. [31] studied the regional variability of RSD along the Equator according to the data collected at four stations in Indonesia. The results indicate that the regional variability of RSD is highly associated with oceanic and continental systems, topographic conditions, and horizontal scale of landmass. Wen et al. [32] investigated seasonal variations of rainfall properties in East China by using a two-dimensional video disdrometer and a vertically pointing micro rain radar. They concluded that summer rainfall is dominated by convective rain, while winter rainfall is completely composed of stratiform rain.

Diurnal variation is the most fundamental cycle of change driven by solar radiation in the Earth's climate system. So far, numerous studies have been conducted on the diurnal variation of the rain spectra worldwide [33–37]. Kozu et al. [33] examined the diurnal and seasonal RSD variations in the maritime continental (Kototabang and Singapore) and inland (Gadanki) stations in the Asian monsoon region. They found that the most pronounced diurnal variation of RSD occurs at Kototabang, which is related to the fact that Kototabang is affected by orographic effect and land-sea thermodynamic differences. Chen et al. [34] studied the diurnal variation of RSD in summer over the Tibetan Plateau. The results indicated that convective rain has large day-night differences, while stratiform rain shows minimal differences. As reported in previous studies, there are distinct differences between the raindrop spectra of summer and winter rainfall over north Taiwan, and both exhibit distinct diurnal variations [35]. RSD in Busan also demonstrates diurnal and seasonal variations [38, 39]. However, few studies have focused on the diurnal variation of RSD in semiarid area of China.

Xinjiang is located in the northwest of China, which is a typical arid and semiarid area. The precipitation characteristics of Xinjiang are significantly different to that in the eastern monsoon region of China [40, 41]. The Ili River Valley is located in the northwest of Xinjiang, where the annual average precipitation is 417.6 mm, which makes it the most humid area in Xinjiang. The Ili River Valley is 360 km long from east to west and 275 km wide from north to south, surrounded by mountains to the north, east, and south with an open "trumpet-shaped" topography to the west. Because of its special geographical location, precipitation in the Ili River Valley presents remarkable diurnal variation. Although microphysical properties of precipitation have been studied in this area, researches about the diurnal variation of RSD are still scarce [42–44]. In this paper, the continuous Parsivel^2 disdrometer measurements from 2020 to 2021 in Zhaosu are used to conduct a comprehensive study on the diurnal variation of RSD and rainfall integral parameters in the Ili River Valley during rainy seasons. The present study aims to advance our understanding of rainfall microphysical processes in arid mountainous region.

The manuscript is organized as follows. Section 2 describes the instruments, data, and methodology used in this study. The diurnal variations of RSD and rainfall integral parameters for different rainfall rates and rain types are detailed in Section 3. Discussion is provided in Section 4. Summary and conclusions are provided in Section 5.

2. Data and Methodology

2.1. Instrument and Data. The RSD data used in this study are collected by a Parsivel^2 disdrometer manufactured by OTT Messtechnik, Germany [45]. The instrument can emit a laser beam with a sampling area of 54 cm^2 and a time interval of 60 s. The particle diameter is determined by the maximum attenuation of the signal, and the fall velocity is estimated from the transit time of the particles within the laser beam. The particles are subdivided into 32 nonequidistant velocity bins ranging from 0.05 to 20.8 m·s^{-1} and 32 nonequidistant size bins ranging from 0.062 to 24.5 mm. As an upgraded version of the first-generation disdrometer Parsivel, the Parsivel^2 disdrometer uses a more expensive laser sensor for the raindrop size and rainfall measurements [46, 47].

This work utilizes two years of disdrometer data during rainy seasons in the Ili River Valley (2020-2021). The instrument is deployed at the meteorological station in Zhaosu (81.09°E, 43.08°N, 1851 m a.m.s.l.). Zhaosu is located in the southwest of the Ili River Valley. The rainfall in the Ili River Valley during rainy seasons is about 200 to 250 mm, and the temperature is usually maintained at 17 ~ 23°C. Easterly and westerly winds occur most frequently in the Ili River Valley, and the wind direction is consistent with the direction of the valley. The synoptic systems affecting the Ili River Valley during rainy seasons are mainly Central Asia low vortex (trough), and the mesoscale systems are mainly mesoscale shear line, mesoscale low pressure, and convective cells. The location of the observation site and the topography of the Ili River Valley are shown in Figure 1. In addition, automatic weather station (AWS) data and ERA5 reanalysis data are also used. AWS can record surface meteorological parameters (temperature, relative humidity, and wind speed) at 1 h sampling intervals. Convective available potential energy (CAPE) is obtained from the ERA5 hourly data on single levels with a horizontal resolution of 0.25° × 0.25°. Based on the above data, this study attempts to illuminate the microphysical and thermodynamic characteristics in the Ili River Valley.

2.2. RSD. Based on disdrometer data, the measured RSD can be calculated as follows:

$$N(D_i) = \frac{1}{S_{\text{eff}}(D_i)\cdot\Delta t\cdot\Delta D_i}\sum_{j=1}^{32}\frac{n_{ij}}{V_j}, \tag{1}$$

where $N(D_i)$ (mm^{-1} m^{-3}) is the number concentration of raindrops per unit volume with diameters between D_i and $D_i+\Delta D_i$; D_i (mm) is the median value of the i^{th} size bin; ΔD_i (mm) is the diameter interval of the i^{th} size bin; Δt (s) is the

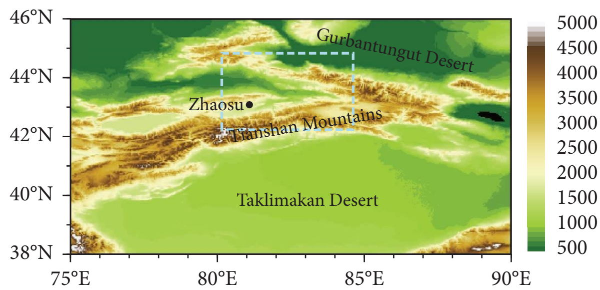

Figure 1: Location of Zhaosu observation site. The blue rectangle represents the Ili River Valley.

sampling time interval; n_{ij} is the number of drops within size bin i and velocity bin j; V_j (m·s^{-1}) is the fall velocity of class j; and $S_{\text{eff}}(D_i)$ (m^2), the effective sampling area, is expressed as $180\,\text{mm} \times (30\,\text{mm-}0.5\ D_i)$.

From the raindrop concentration $N(D_i)$, the integral rainfall parameters including rainfall rate R (mm·h^{-1}), radar reflectivity factor Z (mm^6·m^{-3}), liquid water content W (g·m^{-3}), and total number concentration N_t (m^{-3}) can be calculated by the following equation:

$$R = 6\pi \times 10^{-4} \sum_{i=1}^{32} N(D_i) D_i^3 V(D_i) \Delta D_i,$$

$$Z = \sum_{i=1}^{32} N(D_i) D_i^6 \Delta D_i, \tag{2}$$

$$W = \frac{\pi}{6} \times 10^{-3} \rho_w \sum_{i=1}^{32} N(D_i) D_i^3 \Delta D_i,$$

where ρ_w (g·cm^{-3}) is the density of water.

$$N_t = \sum_{i=1}^{32} N(D_i) \Delta D_i. \tag{3}$$

The three-parameter gamma distribution proposed by Ulbrich [48] has been proven to be a suitable representation of the raindrop spectra and is described as follows:

$$N(D) = N_0 D^{\mu} \exp(-\Lambda D), \tag{4}$$

where N_0 (mm$^{-1-\mu}$ m^{-3}), μ (dimensionless), and Λ (mm^{-1}) are the intercept, shape, and slope parameters of the gamma distribution, respectively. The three parameters in equation (4) can be obtained by using the method of moments [49].

The n-th moment of the RSD is expressed as follows:

$$M_n = \sum_{i=1}^{32} N(D_i) D_i^n \Delta D_i, \tag{5}$$

where the third, fourth, and sixth moments of the size distribution are considered in this study.

Equations (6), (7), and (8) are the three parameters of gamma distribution (μ, Λ, and N_0).

$$\mu = \frac{11G - 8 + \sqrt{G(G+8)}}{2(1-G)} \text{ with } G = \frac{M_4^3}{M_3^2 M_6}, \tag{6}$$

$$\Lambda = (\mu + 4)\frac{M_3}{M_4}, \tag{7}$$

$$N_0 = \frac{\Lambda^{\mu+4} M_3}{\Gamma(\mu+4)}, \tag{8}$$

where $\Gamma(x)$ is the complete gamma function and is described as follows:

$$\Gamma(x) = \sqrt{2\pi} e^{-x} x^{x-1/2}. \tag{9}$$

The normalized gamma distribution has been widely applied to analyze the properties of RSD and the relationships between rainfall integral parameters [50]. In particular, the most important advantage of the normalized gamma distribution is that it is free of any assumption about the shape of the RSD or the relationships between moments of the RSD. In the meantime, it allows observational facts to decide what this shape is and what these relationships are. Here, the model is defined as follows [10]:

$$N(D) = N_w f(\mu) \left(\frac{D}{D_m}\right)^{\mu} \exp\left[-(\mu+4)\frac{D}{D_m}\right], \tag{10}$$

where D_m (mm) and N_w (mm^{-1}·m^{-3}) are the mass-weighted average diameter and the normalized intercept parameter, respectively. D_m, N_w, and $f(\mu)$ are given by the following equation:

$$D_m = \frac{M_4}{M_3},$$

$$N_w = \frac{4^4}{\pi \rho_w}\left(\frac{10^3 W}{D_m^4}\right), \tag{11}$$

$$f(\mu) = \frac{6}{256} \times \frac{(\mu+4)^{\mu+4}}{\Gamma(\mu+4)}.$$

2.3. Data Quality Control. Apart from the inherent limitations of instrument, several quality control (QC) procedures have been applied to the 1-minute disdrometer data to minimize the observation errors. First of all, the lowest two size bins are left empty because of low signal-to-noise ratio. Following Tokay et al. [46], samples with a total number of raindrops smaller than 10 or a disdrometer-derived rainfall rate less than 0.1 mm·h^{-1} are discarded as noise. To focus on rainfall, all samples related to solid precipitation (hail, snow, etc.) are excluded, and raindrops with a diameter larger than 8 mm are also eliminated since they are unrealistic and probably breakup near the ground. As noted by Yuter et al. [51] and Friedrich et al. [52], margin drops caused by particles partially falling within the laser beam as well as unrealistically large and slow falling particles produced by strong winds and splashing effect should be treated as spurious raindrops. In order to further guarantee the reliability of the disdrometer data, raindrops outside ±60% of the empirical fall velocity-diameter relationship proposed by Atlas et al. [53] are discarded from the raw data. Considering the impact of sampling height, before quality control, air-density adjustments are implemented to modify the empirical relationship proposed by Atlas et al. [53] by multiplying the correction factor [34, 54]. The modified relationships are given by the following equations:

$$D = \frac{1}{0.6} \times \ln \frac{10.3}{9.65 - V_t/\delta(h)}, \quad (12)$$

$$\delta(h) = 1 + 3.68 \times 10^{-5} h + 1.71 \times 10^{-9} h^2, \quad (13)$$

where D is the particle diameter, V_t is the fall velocity, h is the sampling height above sea level, and $\delta(h)$ is a correction factor for air-density changes with height.

As shown in Figure 2, the filtered raindrops are mainly below 3 m·s^{-1}, mostly likely related to the "splashing effect." After QC, these unrealistic data are basically removed. Additionally, the definition of an effective rain event proposed by Chen et al. [34] is adopted in this study. Considering most rain events occurring in the Ili River Valley are intermittent, rain events lasting less than 30 min will be excluded to avoid erratic measurements. In this research, May, June, July, August, and September are considered as rainy seasons, since most rainfall occurs from May to September every year. Ultimately, 56 rain events are selected, which include 20918 1 min RSD samples covering the two rainy seasons of 2020-2021 in the Ili River Valley.

3. Results

3.1. Diurnal Variation of Rainfall Integral Parameters. Diurnal variation is one of the most basic modes of global weather and climate system variations, and diurnal variation in precipitation is the most significant among variations of meteorological variables. Precipitation in Zhaosu exhibits an apparent diurnal cycle during rainy seasons. Precipitation mainly occurs in the late afternoon and early evening (Figure 3). The largest contributor to the total rainfall is around 14–19 LST.

Figure 4 displays the time series of mean values of integral rainfall parameters derived from 1-minute disdrometer observations. The time series of R, Z, and W present an obvious multipeak structure. The mean values of R, Z, and W range from 0.67 to 2.64 mm·h^{-1}, 17 to 24.4 dBZ, and 0.06 to 1.14 g·m^{-3}, respectively. The maximum and minimum values of R appear at 19 and 08 LST, respectively. A same variation pattern is found for Z and W. Analysis of the trends of D_m and $\log_{10} N_w$ indicates that the D_m value shows a fluctuating upward trend until 19 LST and then turns to a downward trend, while the $\log_{10} N_w$ value shows an opposite trend. From 14 to 20 LST, the result shows a higher mass-weighted mean diameter D_m (>1.1 mm) and a lower normalized intercept parameter $\log_{10} N_w$ (<3.6). The terminal velocity exhibits an upward trend between 08 and 14 LST, fluctuates around 3.8 m·s^{-1} during 14-00 LST period, and then decreases rapidly. Obviously, the variations in rainfall rate, radar reflectivity, and liquid water content are controlled by the size of raindrops. The terminal velocity of particles also matches with the diameter of raindrops. On the other hand, the significant increase (decrease) in D_m ($\log_{10} N_w$) from afternoon to early evening is probably related to the intensification of collision-coalescence processes, which may be responsible for the rapid growth of raindrop size.

3.2. Diurnal Variation of RSD. In order to explore the diurnal variation of RSD in the Ili River Valley during rainy seasons, each day is divided into four time periods (02–07, 08–13, 14–19, and 20-01 LST). Figure 5 shows the composite raindrop spectra corresponding to these four time periods. In this paper, the classification method proposed by previous researchers is adopted to divide raindrops into three categories: (a) small drops: <1 mm, (b) medium-sized drops: $1 \sim 3$ mm, and (c) large drops: >3 mm [55–57]. The RSD spectra are quite similar at different time periods, showing a unimodal distribution with the peak value appearing around the diameter $D \sim 0.5$ mm. It can be seen that, except for 02–07 LST, the number of small raindrops is almost the same in all the other periods. As the raindrop diameter increases, the variations in RSD spectra start showing up. The concentration of medium and large drops in the period of 14-01 LST is higher than that in the period of 02–13 LST. And this further confirms that the increase in rainfall intensity from the afternoon to early evening is mainly owing to the contribution of medium and large drops.

Figure 6 shows the histograms of different RSD parameters for each defined time period with respect to the entire data set. The histogram of $\log_{10}R$ displays a pronounced unimodal distribution with the peak located at approximately −0.4 in all the periods except for the period of 20-01 LST (Figures 6(a–d)). The statistical characteristics of $\log_{10}R$ show a higher mean and standard deviation at 14–19 LST, indicating that the precipitation variability is stronger. The $\log_{10}W$ histograms in all the four time periods are relatively similar and meet a normal skewness distribution (Figures 6(e–h)). The $\log_{10}W$ frequency distributions for the four periods are concentrated between −2.2 and 0.2 with an almost symmetrical shape. Figures 6(i–l) present a significant diurnal variability of D_m. For the four time periods, the peak value of D_m exists at around 0.8 mm and the frequency rapidly decreases from the peak value as D_m increases. Compared with the other three time periods, the D_m histogram in the 14–19 LST period shows a much wider distribution with a higher frequency when $D_m > 1.8$ mm. The $\log_{10} N_w$ histogram is negatively skewed throughout the day, which displays an inverse distribution to that of D_m (Figures 6(m–p)).

3.3. RSD Properties for Different Rainfall Rates. To better understand the performance of RSD spectra corresponding to different rain intensities from light to heavy, the processed data have been further stratified into five classes on the basis of rainfall rate: $0.1 \le R < 0.5$ mm·h^{-1}, $0.5 \le R < 1$ mm·h^{-1}, $1 \le R < 2$ mm·h^{-1}, $2 \le R < 5$ mm·h^{-1}, and $R \ge 5$ mm·h^{-1}.

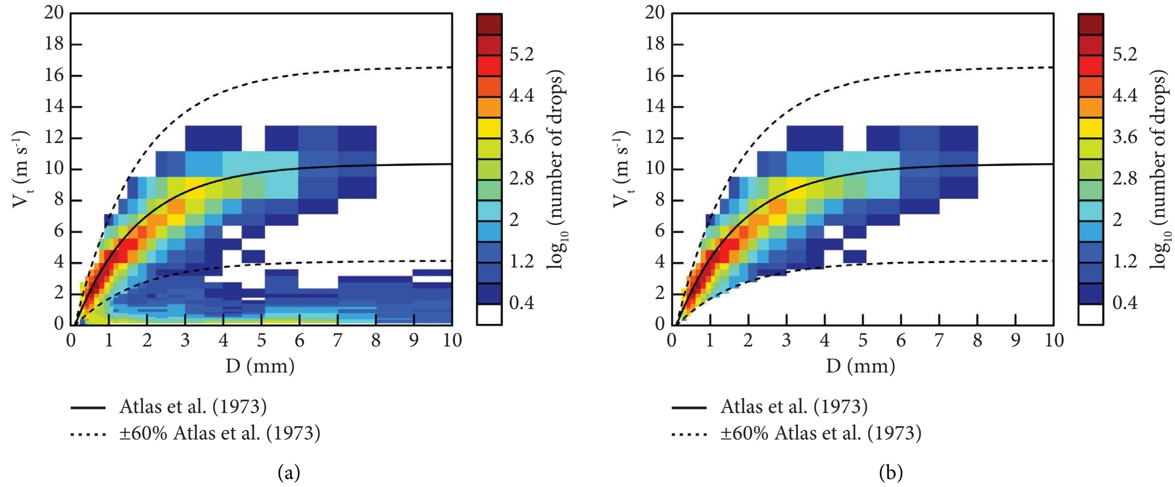

FIGURE 2: Accumulated number of raindrops corresponding to different diameter size and fall velocity bins (a) before and (b) after QC for the entire observation period. The solid lines represent the empirical fall velocity-diameter relationship proposed by Atlas et al. [53] and the air-density adjustment is considered. The dashed lines indicate the ±60% fall velocity-diameter relationship.

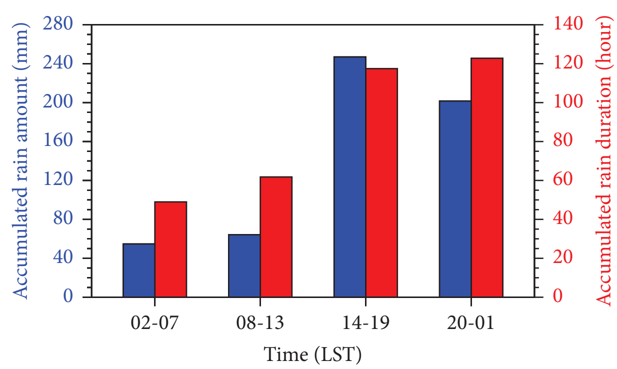

FIGURE 3: Diurnal variations of accumulated rain amount (blue) and rain duration (red).

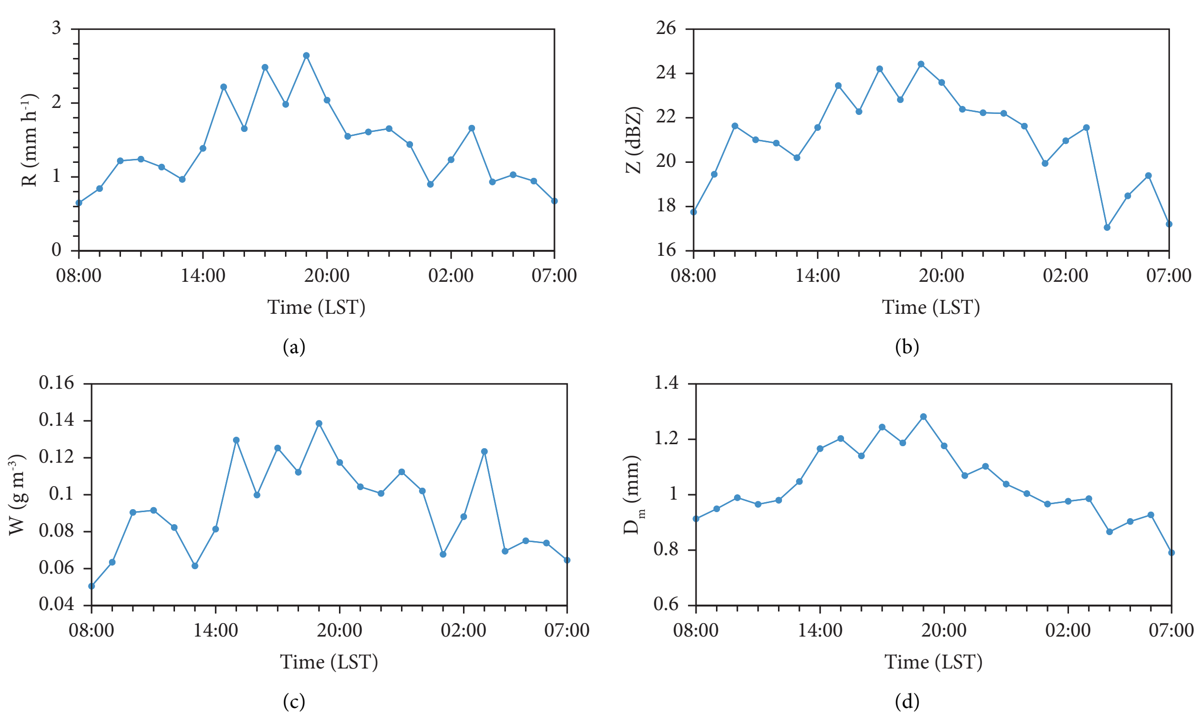

FIGURE 4: Continued.

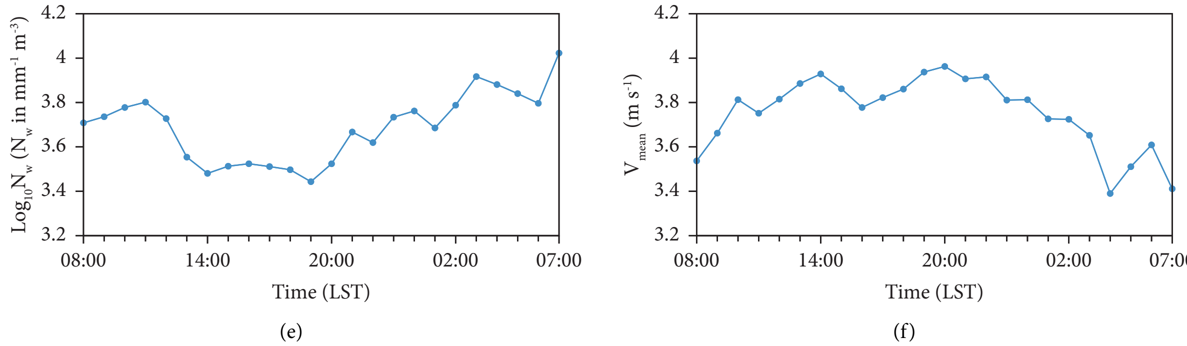

Figure 4: Time series of (a) rainfall rate, R (mm·h^{-1}); (b) radar reflectivity factor, Z (in dBZ = 10log$_{10}Z$); (c) liquid water content, W (g·m^{-3}); (d) mass-weighted average diameter, D_m (mm); (e) normalized intercept parameter, $\log_{10} N_w$ (where N_w is in mm^{-1}·m^{-3}); (f) mean terminal velocity, V_{mean} (m·s^{-1}).

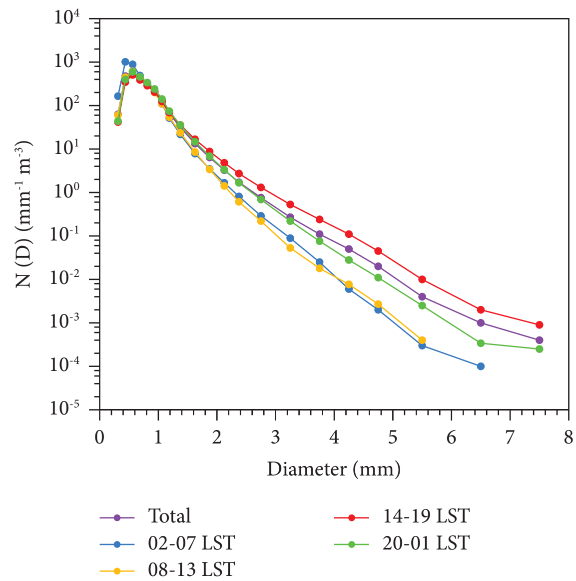

Figure 5: Composite raindrop spectra at different time periods of the day. Dots represent the centre of Parsivel^2 diameter classes.

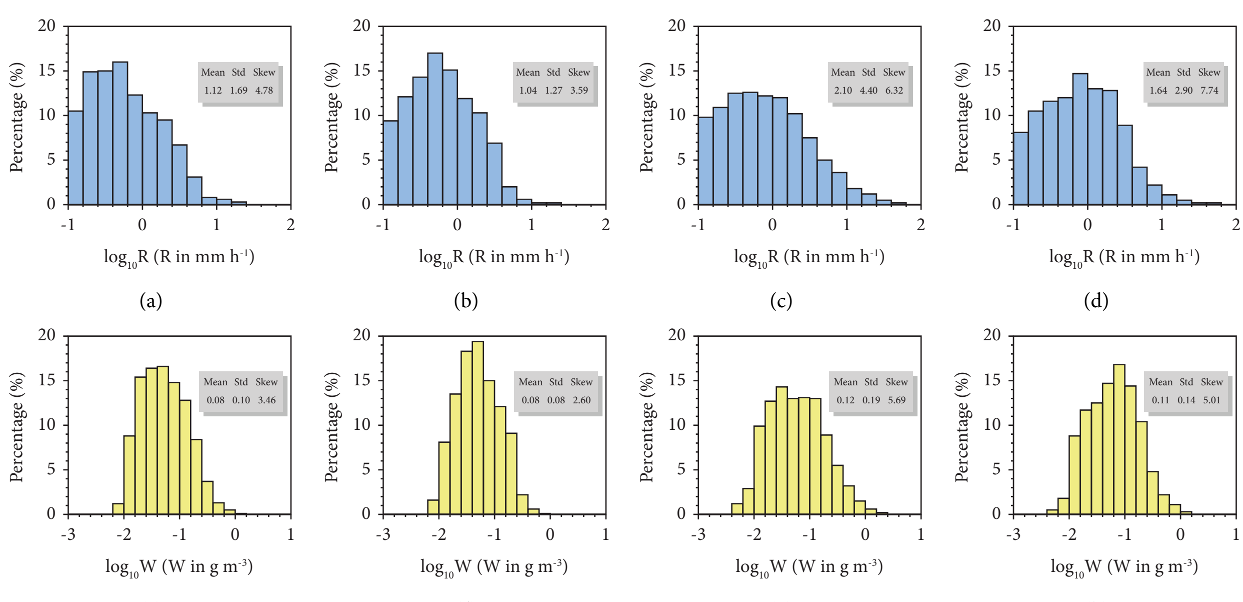

Figure 6: Continued.

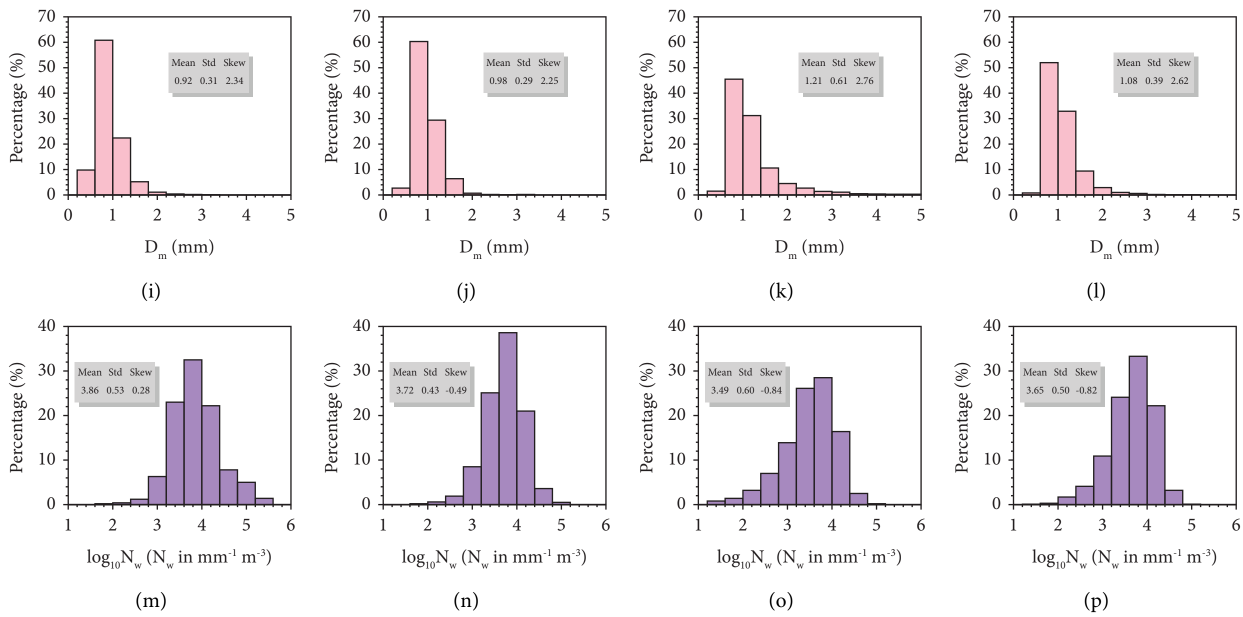

Figure 6: Histograms of different RSD parameters at different time periods of the day: (a–d) rainfall rate, $\log_{10}R$ (where R is in mm·h^{-1}); (e–h) liquid water content, $\log_{10}W$ (where W is in g·m^{-3}); (i–l) mass-weighted average diameter, D_m (mm); (m–p) normalized intercept parameter, $\log_{10} N_w$ (where N_w is in mm^{-1}·m^{-3}). (a, e, i, m): 02–07 LST; (b, f, j, n): 08–13 LST; (c, g, k, o): 14–19 LST; (d, h, l, p): 20-01 LST. Mean values (mean), standard deviation (std), and skewness (skew) are also given in the panels.

Figure 7 shows the diurnal variations of the RSD spectra for the five different rainfall rate classes. The breadth of the RSD shape and the concentration of raindrops in the four time periods increase with increasing rainfall rate at different rainfall rates. In particular, the abundance of small raindrops can be noted in all the periods. The disagreement among the four curves increases significantly when $R \geq 5$ mm·h^{-1}, indicating that the diurnal difference of RSD is more pronounced in the case of high rainfall rates.

The integral rainfall parameters for the five rainfall rate classes at different time periods are summarized in Table 1. The mean value of D_m increases monotonically with increasing rainfall rate in all the four time periods. On the contrary, the shape parameter μ and slope parameter Λ tend to decrease with increasing rainfall intensity. There is no regularity in the variation of $\log_{10} N_w$ within each defined time period. In all rainfall rate classes, the maximum mean D_m value occurs during 14–19 LST, followed by that during 20-01, 08–13, and 02–07 LST. On the contrary, the maximum mean $\log_{10} N_w$ value appears over 02–07 LST, followed by that over 08–13, 20-01, and 14–19 LST. The larger μ values during 02–07 LST indicate that the growth of large diameter particles is suppressed, which may be attributed to weak convective activity in the early morning.

3.4. RSD of Different Rain Types. Natural rainfall is generally divided into two essential types: stratiform and convective precipitation. To divide precipitation into these two types, different researchers have adopted different classification criteria [1, 58]. In this study, the classification procedure of Bringi et al. [1] that is based on the standard deviation of the consecutive rainfall rate (σ_R) is used to distinguish the two precipitation types. For 10 consecutive 1-min RSD samples, samples with $R \geq 0.5$ mm·h^{-1} and $\sigma_R \leq 1.5$ mm·h^{-1} are classified as stratiform rain and samples with $R \geq 5.0$ mm·h^{-1} and $\sigma_R \geq 1.5$ mm·h^{-1} are classified as convective rain. The remaining samples are classified as mixed rain and excluded from the investigation. Using the above classification scheme, 11098 stratiform samples and 1174 convective samples are identified, and results are given in Table 2. In addition, there are 1441 (70), 2156 (32), 3238 (677), and 4263 (395) stratiform (convective) rainfall samples over 02–07, 08–13, 14–19, and 20-01 LST.

Figure 8 shows the diurnal variations of accumulated rain amount and rain duration for stratiform and convective rain types. During the observation period from 2020 to 2021, the accumulated rain amounts of stratiform and convective rain are 255.2 and 199.3 mm, respectively, while the occurrence times of stratiform and convective rain are 180.52 and 19.56 h, respectively. Despite the negligible contribution of convective precipitation to the total rain duration, its contribution to the accumulated rain amount is significant. Differences in the diurnal cycle between the two rain types are also observed. Stratiform precipitation in Zhaosu can occur at any time of the day, and the maximum accumulated rain amount of stratiform precipitation occurs at 20-01 LST. Convective precipitation in Zhaosu mainly occurs during the late afternoon and early evening when convection is active, and the maximum accumulated rain amount of convective precipitation occurs at 14–19 LST.

To further understand the RSD characteristics of different rain types, Figure 9 shows the composite raindrop spectra for stratiform and convective rain types over different time periods. Although the RSDs in the four time periods exhibit a similar distribution for the same rain type,

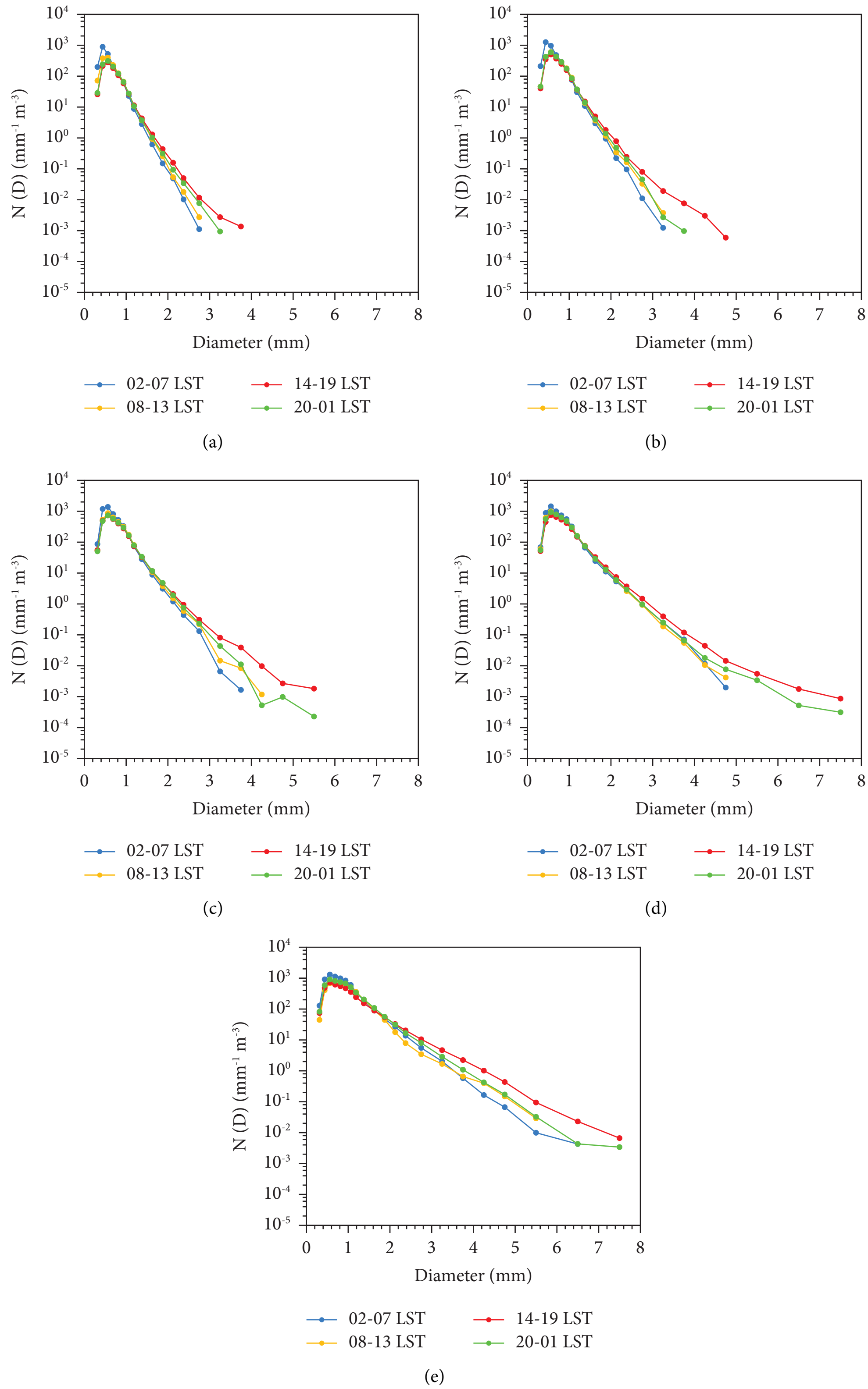

Figure 7: Composite raindrop spectra for the five rainfall rate classes at different time periods of the day. The rainfall rate intervals are (in mm·h^{-1}) (a) $0.1 \leq R < 0.5$, (b) $0.5 \leq R < 1$, (c) $1 \leq R < 2$, (d) $2 \leq R < 5$, and (e) $R \geq 5$.

Table 1: Mean values of R, D_m, $\log_{10} N_w$, μ, and Λ for the five rainfall rate classes at different time periods of the day.

	Class (mm·h^{-1})	No. of 1-min samples	R (mm·h^{-1})	D_m (mm)	$\log_{10} N_w$ (N_w in mm^{-1}·m^{-3})	μ	Λ (mm^{-1})
02–07 LST	$0.1 \le R < 0.5$	1419	0.26	0.78	3.77	14.43	26.40
	$0.5 \le R < 1$	602	0.70	0.89	3.95	10.93	18.94
	$1 \le R < 2$	453	1.43	1.00	4.00	9.89	16.02
	$2 \le R < 5$	387	3.01	1.24	3.90	8.06	11.88
	$R \ge 5$	78	8.68	1.62	3.82	5.53	6.69
08–13 LST	$0.1 \le R < 0.5$	1634	0.27	0.84	3.62	12.44	21.24
	$0.5 \le R < 1$	885	0.71	0.96	3.76	8.94	14.44
	$1 \le R < 2$	642	1.43	1.08	3.83	6.99	11.12
	$2 \le R < 5$	493	2.93	1.27	3.81	4.54	7.37
	$R \ge 5$	55	7.54	1.71	3.68	6.12	6.65
14–19 LST	$0.1 \le R < 0.5$	2755	0.26	0.92	3.38	13.36	21.14
	$0.5 \le R < 1$	1286	0.72	1.08	3.57	9.42	14.08
	$1 \le R < 2$	1245	1.44	1.22	3.66	7.30	10.69
	$2 \le R < 5$	996	3.13	1.48	3.60	5.97	7.71
	$R \ge 5$	686	11.77	2.18	3.33	5.62	5.41
20-01 LST	$0.1 \le R < 0.5$	2614	0.26	0.89	3.47	13.28	21.18
	$0.5 \le R < 1$	1544	0.73	0.98	3.72	9.28	14.86
	$1 \le R < 2$	1439	1.44	1.13	3.75	6.88	10.71
	$2 \le R5$	1283	2.99	1.32	3.77	5.21	7.89
	$R \ge 5$	422	10.09	1.75	3.70	5.14	6.00

Table 2: Mean values of R, D_m, $\log_{10} N_w$, μ, and Λ for stratiform and convective rain types at different time periods of the day.

	Rain type	No. of 1 min samples	R (mm·h^{-1})	D_m (mm)	$\log_{10} N_w$ (N_w in mm^{-1}·m^{-3})	μ	Λ (mm^{-1})
02–07 LST	Stratiform	1441	1.42	0.98	3.96	10.32	17.25
	Convective	70	7.78	1.65	3.67	6.04	7.06
08–13 LST	Stratiform	2156	1.31	1.04	3.77	7.63	12.50
	Convective	32	7.89	1.70	3.71	6.95	7.50
14–19 LST	Stratiform	3238	1.32	1.11	3.65	8.44	12.76
	Convective	677	10.48	2.06	3.28	5.80	6.14
20-01 LST	Stratiform	4263	1.45	1.09	3.73	7.64	12.33
	Convective	395	9.18	1.67	3.68	6.48	7.56

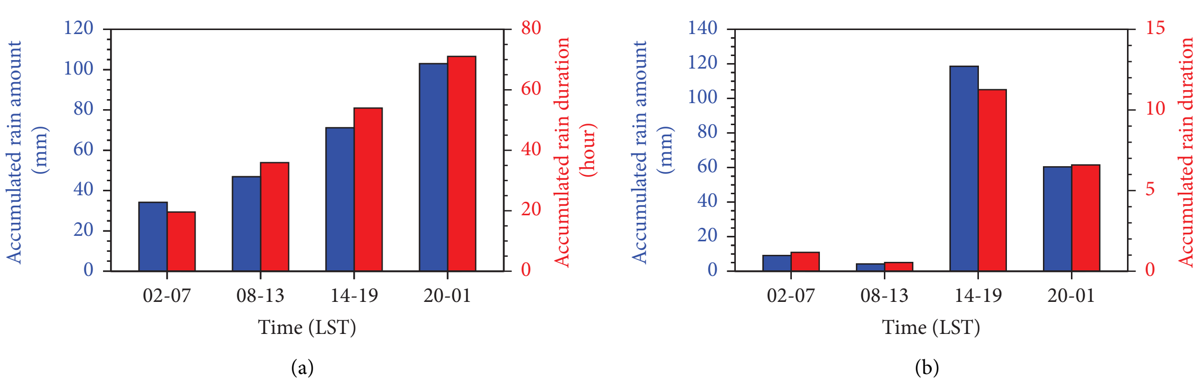

Figure 8: Diurnal variations of accumulated rain amount (blue) and rain duration (red) for (a) stratiform and (b) convective rain types.

clear differences in the RSDs can be found between stratiform and convective rain types. The RSD in stratiform rainfall shows a steep slope, while that in convective rainfall shows a gentle slope. Compared to that for stratiform precipitation, the mean RSD for convective rain type has a wider and flatter spectral width. For both stratiform and convective precipitation, the maximum raindrop diameter appears over 14–19 LST. The spectra indicate that convective precipitation has a higher number concentration of medium and large drops than stratiform precipitation, which may be attributed to the collisional breakup of large raindrops in convective rainfall [7]. For stratiform precipitation, the four curves agree well with each other for raindrop sizes smaller than 4 mm. In contrast, the concentration of raindrops larger than 4 mm is significantly higher during 14–19 and 20-01 LST. For convective precipitation, the gap between the four curves gradually widens when the raindrop diameter is greater than 2 mm, and the raindrop number concentration in the afternoon is significantly higher than in other time of the day. Table 2 lists the statistics of rain parameters for the two rain types at different time periods. From the table, it can be found that the mass-weighted average diameter D_m for convective rain is larger than that for stratiform rain. In contrast, the mean $\log_{10} N_w$, μ, and Λ values of stratiform rain are higher than those of convective rain.

3.5. Distributions of D_m and N_w. Figure 10 depicts the distributions of $\log_{10} N_w$ versus D_m for stratiform and convective rain in the four time periods. The two black rectangles correspond to the maritime and continental convective clusters, and the black dashed line is a separation line between stratiform and convective rain proposed by Bringi et al. [1]. In the case of maritime convective cluster, the D_m values are scattered from 1.5 to 1.75 mm, and the $\log_{10} N_w$ values are between 4 and 4.5. And the D_m values of continental convective cluster are distributed between 2 and 2.75 mm, and the $\log_{10} N_w$ values are concentrated between 3 and 3.5. The mean D_m ($\log_{10} N_w$) values for convective rain are about 1.65 (3.67), 1.7 (3.71), 2.06 (3.28), and 1.67 (3.68) in the periods of 02–07, 08–13, 14–19, and 20-01 LST, respectively, which are larger (lower) than their counterparts for stratiform rain during the same time period. The mean D_m-$\log_{10} N_w$ pairs differ significantly in the diurnal cycle for stratiform and convective rain types. For stratiform rain, most points are concentrated in the region with lower D_m and higher $\log_{10} N_w$. It is found that the stratiform rain over 02–07 LST has the highest mean value of $\log_{10} N_w$ and the lowest mean value of D_m. Chen et al. [34] analyzed three-year disdrometer data over the central Tibetan Plateau and found that convective daytime rain could be identified as continental-like rain, while convective rain at night could be identified as maritime-like rain. Figure 10 demonstrates that the convective rain in the Ili River Valley over 14–19 LST can be characterized as the continental convective cluster, while in the rest time of the day, it is neither in the maritime cluster nor in the continental cluster.

3.6. Z-R Relationship. The power-law relationship between radar reflectivity factor Z and rainfall rate R ($Z = A \cdot R^b$) is the most widely used method for single-polarization radar QPE. Establishing a suitable Z-R relationship can minimize the uncertainties in radar QPE for a certain area. Figure 11 shows the scatter plots of Z versus R, as well as the fitting power-law relationships for stratiform and convective rain types. The Z-R relationships for stratiform and convective rain are $Z = 123.53R^{1.73}$ and $Z = 97.08R^{1.85}$, respectively. The empirical relationship of $Z = 300R^{1.4}$ is commonly used in the Next-Generation Weather Radar (NEXRAD) for convective precipitation [59], and the empirical relationship of $Z = 200R^{1.6}$ is recommended in midlatitude areas for stratiform precipitation [60]. The fitting curve of stratiform precipitation in Zhaosu is basically coincident with the fitting curve of stratiform precipitation in midlatitude areas, and there is not much difference in the estimation of rainfall between the two relationships (Figure 11(a)). The empirical relationship ($Z = 300R^{1.4}$) underestimates the convective rain at a rainfall rate below 12 mm·h^{-1}, while it overestimates the convective rain at a rainfall rate above 12 mm·h^{-1}. In other words, the default NEXRAD relationship may increase the uncertainty of QPE.

4. Discussion

Many studies have indicated that the diurnal variation of RSD characteristics is not a random behaviour. It is closely related to microphysical processes and environment factors [5, 61]. To explore the mechanisms for the observed diurnal variation of RSD in the Ili River Valley, temperature (°C), relative humidity (%), wind speed (m·s^{-1}), and CAPE (J·kg^{-1}) obtained from the automatic weather station (AWS) data and ERA5 reanalysis data for the rainy seasons of 2020-2021 in Zhaosu are employed in the present study. As shown in Figure 12, temperature, humidity, wind speed, and CAPE have obvious diurnal variation characteristics. Temperature and wind speed remain low from the nighttime to early morning, then gradually increase and reach their peaks in the late afternoon. Relative humidity, however, shows an opposite trend. Lower temperature and wind speed are not conducive to the evaporation and collision of small raindrops, which may be one of the reasons for the abundance of small raindrops and the lack of large and medium raindrops in the midnight and early morning. From 08 LST, temperature gradually increases while the heating effect of solar radiation increases the atmospheric instability, and CAPE begins to accumulate. In addition, due to the topography blocking effect, low-level airflows converge at the foot of the mountain and ascend along the windward slope, triggering convective activities. The trumpet-shaped topography in the Ili River Valley allows the warm moist airflow from the Atlantic Ocean to converge there, and the abundant water vapour is conducive to the maintenance and enhancement of convection. In the afternoon, shortwave solar radiation intensifies sharply, ascending motion further develops, pressure decreases, and wind speed increases significantly. When CAPE gets released at 17 : 00, precipitation reaches an intense stage. The precipitation gradually decays afterwards, resulting in more stratiform rainfall from the anvil clouds. Strong ascending motion and uneven heating of the land surface can prolong the interaction time of particles and provide a favourable condition for collision-coalescence processes of particles, causing them to grow bigger in size. This process is sometimes referred to as drop sorting [5, 62]. This helps to explain the higher concentration of

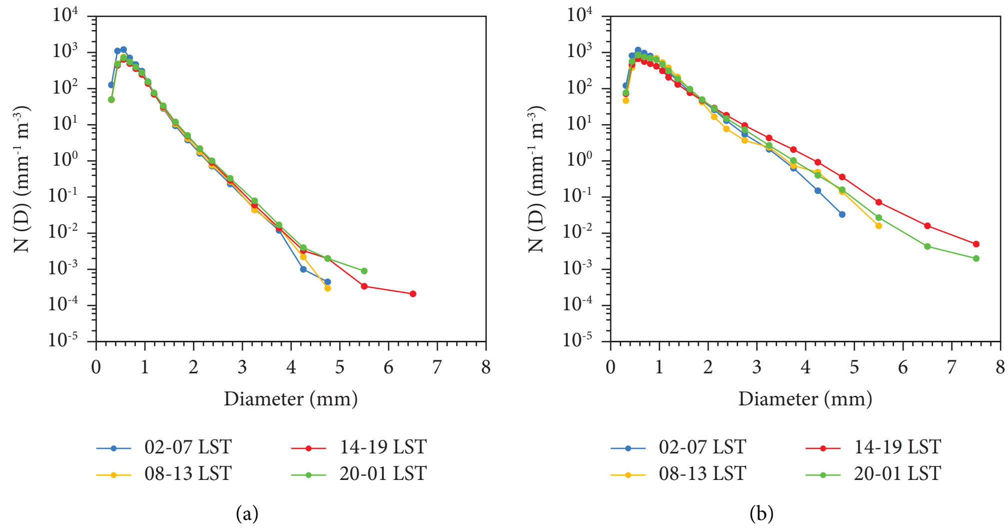

FIGURE 9: Composite raindrop spectra for stratiform and convective rain types at different time periods of the day.

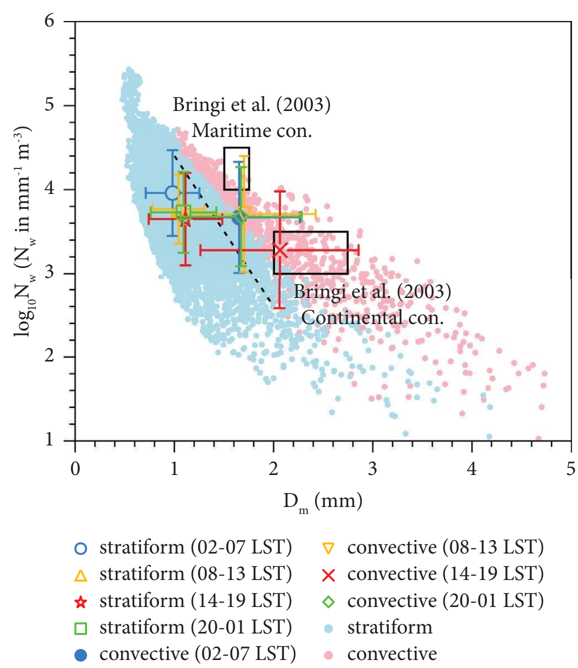

FIGURE 10: Scatter plots of $\log_{10} N_w$ (where N_w is in $mm^{-1}{\cdot}m^{-3}$) versus D_m (mm) for stratiform (light blue dots) and convective (light pink dots) rain types. The two black rectangles correspond to the maritime and continental convective clusters and the black dashed line is a separation line between stratiform and convective rain proposed by Bringi et al. [1]. The average values of $\log_{10} N_w$ and D_m (along with plus-minus standard deviation) for stratiform and convective rain types at different time periods are distinguished by different symbols and explained in the legend.

medium and large raindrops from the afternoon to early evening. At the same time, the warmer and drier environment accelerates the evaporation of small raindrops, and the processes of collision-coalescence will also capture a large number of small particles, leading to a significant decrease in the concentration of small raindrops. Note that the findings of this work are based on observations from a single measurement instrument. Different types of advanced observation instruments should also be used to further study the microphysical characteristics of clouds and precipitation in the Ili River Valley.

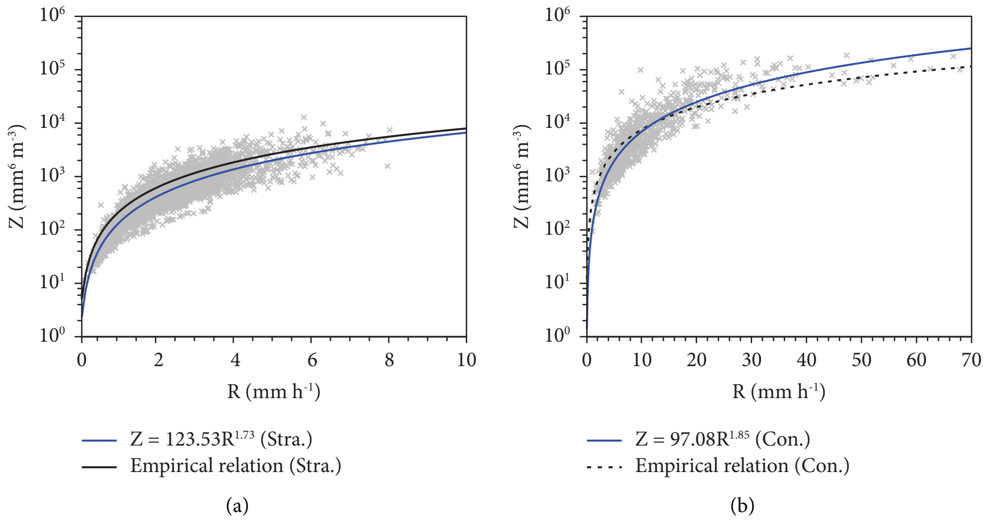

FIGURE 11: Scatter plots of Z (mm^6·m^{-3}) versus R (mm·h^{-1}) for stratiform and convective rain types. The solid blue lines indicate the fitting power-law relationships in Zhaosu. The black solid line and black dashed line, respectively, represent the empirical relationships ($Z = 200R^{1.60}$ for stratiform rain type and $Z = 300R^{1.40}$ for convective rain type).

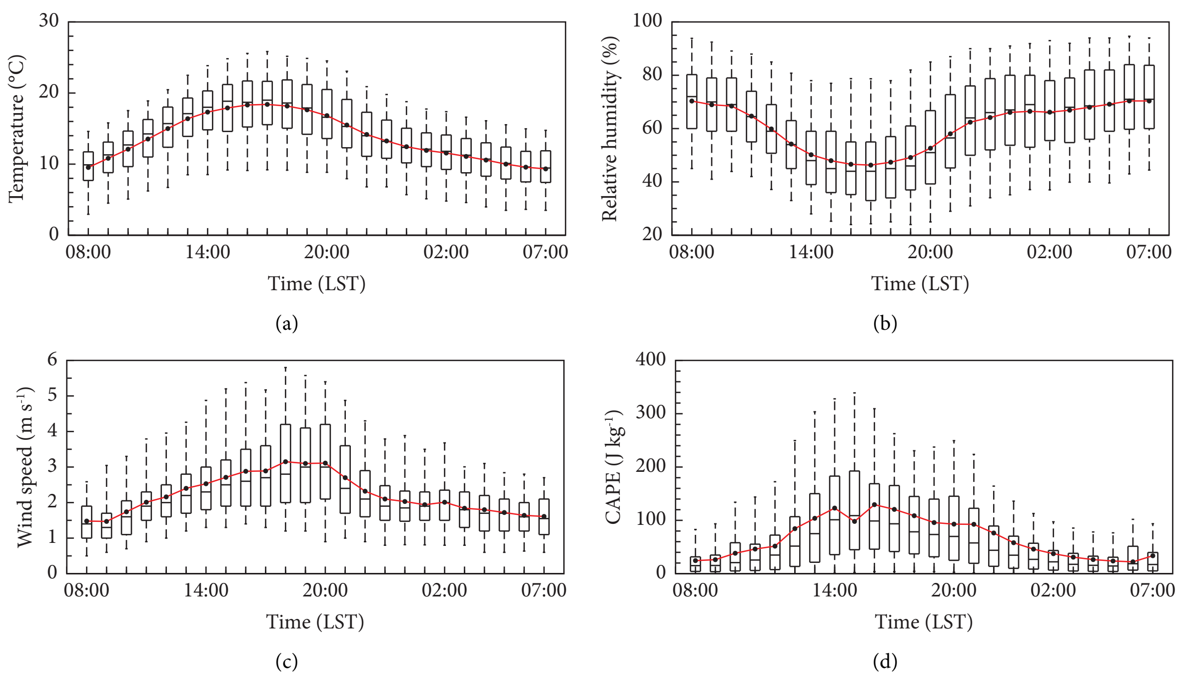

FIGURE 12: Diurnal variations of (a) temperature (°C), (b) relative humidity (%), (c) wind speed (m·s^{-1}), and (d) CAPE (J·kg^{-1}) during the observation period calculated from automatic weather station data and ERA5 reanalysis data. The central line of the box indicates the median, and the bottom and top lines of the box indicate the 25th and 75th percentiles, respectively. The bottom and top of the dashed vertical lines indicate the 5th and 95th percentiles, respectively. Red solid lines represent the mean values.

5. Summary and Conclusions

In this study, the diurnal variation of RSD for different rainfall rate categories and different rain types in the Ili River Valley during rainy seasons from 2020 to 2021 is investigated using observations of a Parsivel^2 disdrometer. Integral rainfall and gamma parameters are also investigated to interpret possible microphysical processes associated with the RSD. The main conclusions are as follows:

(1) There are significant diurnal differences in precipitation and RSD in Zhaosu during rainy seasons. Precipitation mainly occurs in the late afternoon and early evening. The variations in rainfall rate, radar reflectivity, and liquid water content are controlled by the size of raindrops. The increase in rainfall intensity from the afternoon to early evening is mainly owing to the contribution of medium and large drops.

(2) The RSD exhibits diurnal differences between different rainfall rate classes; the diurnal difference of RSD is more pronounced in the case of high rainfall rates. In all rainfall rate classes, the RSDs in 14–19 LST have higher mass-weighted mean diameter and lower normalized intercept parameter than in other time of the day.

(3) Stratiform precipitation can occur at any time of the day, yet convective precipitation mainly occurs during the late afternoon and early evening. The convective spectrum has a higher number concentration of medium and large drops than that of stratiform rainfall in all the four time periods. Convective rain in the Ili River Valley over 14–19 LST can be characterized as the continental convective cluster, while in the rest time of the day it is neither in the maritime cluster nor in the continental cluster.

(4) The fitting curve of stratiform precipitation in Zhaosu is basically coincident with the empirical relationship of $Z = 200R^{1.6}$. The empirical relationship ($Z = 300R^{1.4}$) underestimates the convective rain when $R < 12\,\mathrm{mm{\cdot}h^{-1}}$, while it overestimates the convective rain when $R > 12\,\mathrm{mm{\cdot}h^{-1}}$.

(5) The possible mechanisms responsible for the diurnal variation of RSD are discussed. Distinct differences in temperature, relative humidity, wind speed, and CAPE may be responsible for the diurnal variation characteristics of RSD.

Data Availability

The data used to support the findings of this study are available from the corresponding author upon request.

Conflicts of Interest

The authors declare that they have no conflicts of interest regarding the publication of this paper.

Acknowledgments

This study was funded by the Natural Science Foundation of Xinjiang Uygur Autonomous Region (Grant no. 2022D01B75), the National Natural Science Foundation of China (Grant no. U2003106), Science and Technology Innovation Development Fund Project of Xinjiang Meteorological Bureau (Grant no. MS202210), Tianshan Mountains Talent Project (Grant no. 2022TSYCLJ0003), S&T Development Fund of IDM (Grant nos. KJFZ202301 and KJFZ202303), and the Natural Science Foundation of Xinjiang Uygur Autonomous Region (Grant no. 2022D01B227).

References

[1] V. N. Bringi, V. Chandrasekar, J. Hubbert, E. Gorgucci, W. L. Randeu, and M. Schoenhuber, "Raindrop size distribution in different climatic regimes from disdrometer and dual-polarized radar analysis," *Journal of the Atmospheric Sciences*, vol. 60, no. 2, pp. 354–365, 2003.

[2] C. W. Ulbrich and D. Atlas, "Microphysics of raindrop size spectra: tropical continental and maritime storms," *Journal of Applied Meteorology and Climatology*, vol. 46, no. 11, pp. 1777–1791, 2007.

[3] K. Chakravarty and P. E. Raj, "Raindrop size distributions and their association with characteristics of clouds and precipitation during monsoon and post-monsoon periods over a tropical Indian station," *Atmospheric Research*, vol. 124, pp. 181–189, 2013.

[4] F. S. Marzano, D. Cimini, and M. Montopoli, "Investigating precipitation microphysics using ground-based microwave remote sensors and disdrometer data," *Atmospheric Research*, vol. 97, no. 4, pp. 583–600, 2010.

[5] D. Rosenfeld and C. W. Ulbrich, "Cloud microphysical properties, processes, and rainfall estimation opportunities," *Meteorological Monographs*, vol. 30, no. 52, p. 237, 2003.

[6] A. Thomas, V. P. Kanawade, K. Chakravarty, and A. K. Srivastava, "Characterization of raindrop size distributions and its response to cloud microphysical properties," *Atmospheric Research*, vol. 249, Article ID 105292, 2021.

[7] Z. Hu and R. C. Srivastava, "Evolution of raindrop size distribution by coalescence, breakup, and evaporation: theory and observations," *Journal of the Atmospheric Sciences*, vol. 52, no. 10, pp. 1761–1783, 1995.

[8] D. Atlas and C. W. Ulbrich, "An observationally based conceptual model of warm oceanic convective rain in the tropics," *Journal of Applied Meteorology*, vol. 39, no. 12, pp. 2165–2181, 2000.

[9] A. A. Jensen, J. Y. Harrington, and H. Morrison, "Microphysical characteristics of squall-line stratiform precipitation and transition zones simulated using an ice particle property-evolving model," *Monthly Weather Review*, vol. 146, no. 3, pp. 723–743, 2018.

[10] V. N. Bringi and V. Chandrasekar, *Polarmetric Doppler Weather Radar: Principles and Applications*, Cambridge University Press, Cambridge, UK, 2001.

[11] G. Zhang, J. Sun, and E. A. Brandes, "Improving parameterization of rain microphysics with disdrometer and radar observations," *Journal of the Atmospheric Sciences*, vol. 63, no. 4, pp. 1273–1290, 2006.

[12] B. Chapon, G. Delrieu, M. Gosset, and B. Boudevillain, "Variability of raindrop size distribution and its effect on the *Z-R* relationship: a case study for intense Mediterranean rainfall," *Atmospheric Research*, vol. 87, no. 1, pp. 52–65, 2008.

[13] R. Cifelli, V. Chandrasekar, H. N. Chen, and L. E. Johnson, "High resolution radar quantitative precipitation estimation in the San Francisco bay area: rainfall monitoring for the urban environment," *Journal of the Meteorological Society of Japan*, vol. 96, no. 0, pp. 141–155, 2018.

[14] M. S. Gilmore, J. M. Straka, and E. N. Rasmussen, "Precipitation uncertainty due to variations in precipitation particle parameters within a simple microphysics scheme," *Monthly Weather Review*, vol. 132, no. 11, pp. 2610–2627, 2004.

[15] C. Cohen and E. W. McCaul Jr., "The sensitivity of simulated convective storms to variations in prescribed single-moment microphysics parameters that describe particle distributions, sizes, and numbers," *Monthly Weather Review*, vol. 134, no. 9, pp. 2547–2565, 2006.

[16] G. M. McFarquhar, T.-L. Hsieh, M. Freer, J. Mascio, and B. F. Jewett, "The characterization of ice hydrometeor gamma size distributions as volumes in N_0-λ-μ phase space:

implications for microphysical process modeling," *Journal of the Atmospheric Sciences*, vol. 72, no. 2, pp. 892–909, 2015.

[17] Y. Wu and L. Liu, "Statistical characteristics of raindrop size distribution in the Tibetan Plateau and southern China," *Advances in Atmospheric Sciences*, vol. 34, no. 6, pp. 727–736, 2017.

[18] C. Salles, J. Poesen, and D. Sempere-Torres, "Kinetic energy of rain and its functional relationship with intensity," *Journal of Hydrology*, vol. 257, no. 1-4, pp. 256–270, 2002.

[19] M. Angulo-Martinez and A. P. Barros, "Measurement uncertainty in rainfall kinetic energy and intensity relationships for soil erosion studies: an evaluation using PARSIVEL disdrometers in the Southern Appalachian Mountains," *Geomorphology*, vol. 228, no. 1, pp. 28–40, 2015.

[20] F. G. Carollo, V. Ferro, and M. A. Serio, "Estimating rainfall erosivity by aggregated drop size distributions," *Hydrological Processes*, vol. 30, no. 13, pp. 2119–2128, 2016.

[21] K. Nanko, S. M. Moskalski, and R. Torres, "Rainfall erosivity–intensity relationships for normal rainfall events and a tropical cyclone on the US southeast coast," *Journal of Hydrology*, vol. 534, pp. 440–450, 2016.

[22] Q. Cao, G. Zhang, E. Brandes, T. Schuur, A. Ryzhkov, and K. Ikeda, "Analysis of video disdrometer and polarimetric radar data to characterize rain microphysics in Oklahoma," *Journal of Applied Meteorology and Climatology*, vol. 47, no. 8, pp. 2238–2255, 2008.

[23] B. Radhakrishna, T. N. Rao, D. N. Rao, N. P. Rao, K. Nakamura, and A. K. Sharma, "Spatial and seasonal variability of raindrop size distributions in southeast India," *Journal of Geophysical Research: Atmospheres*, vol. 114, no. D4, Article ID D04203, 2009.

[24] B. Chen, J. Yang, and J. Pu, "Statistical characteristics of raindrop size distribution in the Meiyu season observed in Eastern China," *Journal of the Meteorological Society of Japan*, vol. 91, no. 2, pp. 215–227, 2013.

[25] Q. Tang, H. Xiao, C. Guo, and L. Feng, "Characteristics of the raindrop size distributions and their retrieved polarimetric radar parameters in northern and southern China," *Atmospheric Research*, vol. 135-136, no. 1, pp. 59–75, 2014.

[26] A. R. Jameson, M. L. Larsen, and A. B. Kostinski, "Disdrometer network observations of finescale spatial-temporal clustering in rain," *Journal of the Atmospheric Sciences*, vol. 72, no. 4, pp. 1648–1666, 2015.

[27] Q. W. Zeng, Y. Zhang, H. C. Lei et al., "Microphysical characteristics of precipitation during pre-monsoon, monsoon, and post-monsoon periods over the South China Sea," *Advances in Atmospheric Sciences*, vol. 36, no. 10, pp. 1103–1120, 2019.

[28] L. Luo, J. Guo, H. N. Chen et al., "Microphysical characteristics of rainfall observed by a 2DVD disdrometer during different seasons in Beijing, China," *Remote Sensing*, vol. 13, no. 12, p. 2303, 2021.

[29] L. Feng, X. T. Liu, H. Xiao et al., "Characteristics of raindrop size distribution in Typhoon Nida (2016) before and after landfall in southern China from 2D video disdrometer data," *Advances in Meteorology*, vol. 2021, no. 1, Article ID 9349738, 14 pages, 2021.

[30] B. Dolan, B. Fuchs, S. A. Rutledge, E. A. Barnes, and E. J. Thompson, "Primary modes of global drop size distributions," *Journal of the Atmospheric Sciences*, vol. 75, no. 5, pp. 1453–1476, 2018.

[31] M. Marzuki, H. Hashiguchi, M. K. Yamamoto, S. Mori, and M. D. Yamanaka, "Regional variability of raindrop size distribution over Indonesia," *Annales Geophysicae*, vol. 31, no. 11, pp. 1941–1948, 2013.

[32] L. Wen, K. Zhao, M. Y. Wang, and G. F. Zhang, "Seasonal variations of observed raindrop size distribution in East China," *Advances in Atmospheric Sciences*, vol. 36, no. 4, pp. 346–362, 2019.

[33] T. Kozu, K. K. Reddy, S. Mori et al., "Seasonal and diurnal variations of raindrop size distribution in Asian monsoon region," *Journal of the Meteorological Society of Japan*, vol. 84, pp. 195–209, 2006.

[34] B. J. Chen, Z. Q. Hu, L. P. Liu, and G. F. Zhang, "Raindrop size distribution measurements at 4,500 m on the Tibetan Plateau during TIPEX-III," *Journal of Geophysical Research: Atmospheres*, vol. 122, no. 20, pp. 11092–11106, 2017.

[35] B. K. Seela, J. Janapati, P.-L. Lin, P. K. Wang, and M.-T. Lee, "Raindrop size distribution characteristics of summer and winter season rainfall over north Taiwan," *Journal of Geophysical Research: Atmospheres*, vol. 123, no. 20, pp. 11602–11624, 2018.

[36] Y. Ma, G. H. Ni, C. V. Chandra, F. Q. Tian, and H. N. Chen, "Statistical characteristics of raindrop size distribution during rainy seasons in the Beijing urban area and implications for radar rainfall estimation," *Hydrology and Earth System Sciences*, vol. 23, no. 10, pp. 4153–4170, 2019.

[37] E. Villalobos-Puma, D. Martinez-Castro, J. Flores-Rojas, M. Saavedra-Huanca, and Y. Silva-Vidal, "Diurnal cycle of raindrops size distribution in a Valley of the Peruvian Central Andes," *Atmosphere*, vol. 11, no. 1, p. 38, 2019.

[38] C.-H. You and D.-I. Lee, "Decadal variation in raindrop size distributions in Busan, Korea," *Advances in Meteorology*, vol. 2015, no. 1, Article ID 329327, 8 pages, 2015.

[39] S.-H. Suh, C.-H. You, and D.-I. Lee, "Climatological characteristics of raindrop size distributions in Busan, Republic of Korea," *Hydrology and Earth System Sciences*, vol. 20, no. 1, pp. 193–207, 2016.

[40] W. Huang, S. Feng, J. Chen, and F. Chen, "Physical mechanisms of summer precipitation variations in the Tarim basin in northwestern China," *Journal of Climate*, vol. 28, no. 9, pp. 3579–3591, 2015.

[41] J. Yao, W. Mao, J. Chen, and T. Dilinuer, "Recent signal and impact of wet-to-dry climatic shift in Xinjiang, China," *Journal of Geographical Sciences*, vol. 31, no. 9, pp. 1283–1298, 2021.

[42] Y. Zeng, L. Yang, Z. Tong et al., "Statistical characteristics of raindrop size distribution during rainy seasons in northwest China," *Advances in Meteorology*, vol. 2021, no. 1, Article ID 6667786, 12 pages, 2021.

[43] Y. Zeng, J. Li, L. Yang et al., "Microphysical characteristics of raindrop size distribution and implications for dual-polarization radar quantitative precipitation estimations in the Tianshan Mountains, China," *Remote Sensing*, vol. 15, no. 10, pp. 2668–2719, 2023.

[44] Y. Jiang, L. Yang, Y. Zeng et al., "Comparison of summer raindrop size distribution characteristics in the western and central Tianshan Mountains of China," *Meteorological Applications*, vol. 29, no. 3, p. e2067, 2022.

[45] M. Löffler-Mang and J. Joss, "An optical disdrometer for measuring size and velocity of hydrometeors," *Journal of Atmospheric and Oceanic Technology*, vol. 17, no. 2, pp. 130–139, 2000.

[46] A. Tokay, W. A. Petersen, P. Gatlin, and M. Wingo, "Comparison of raindrop size distribution measurements by collocated disdrometers," *Journal of Atmospheric and Oceanic Technology*, vol. 30, no. 8, pp. 1672–1690, 2013.

[47] A. Tokay, D. B. Wolff, and W. A. Petersen, "Evaluation of the new version of the laser-optical disdrometer, OTT Parsivel^2," *Journal of Atmospheric and Oceanic Technology*, vol. 31, no. 6, pp. 1276–1288, 2014.

[48] C. W. Ulbrich, "Natural variations in the analytical form of the raindrop size distribution," *Journal of Climate and Applied Meteorology*, vol. 22, no. 10, pp. 1764–1775, 1983.

[49] A. Tokay and D. A. Short, "Evidence from tropical raindrop spectra of the origin of rain from stratiform versus convective clouds," *Journal of Applied Meteorology*, vol. 35, no. 3, pp. 355–371, 1996.

[50] J. Testud, S. Oury, R. A. Black, P. Amayenc, and X. Dou, "The concept of "normalized" distribution to describe raindrop spectra: a tool for cloud physics and cloud remote sensing," *Journal of Applied Meteorology*, vol. 40, no. 6, pp. 1118–1140, 2001.

[51] S. E. Yuter, D. E. Kingsmill, L. B. Nance, and M. LöfflerMang, "Observations of precipitation size and fall speed characteristics within coexisting rain and wet snow," *Journal of Applied Meteorology and Climatology*, vol. 45, no. 10, pp. 1450–1464, 2006.

[52] K. Friedrich, S. Higgins, F. J. Masters, and C. R. Lopez, "Articulating and stationary PARSIVEL disdrometer measurements in conditions with strong winds and heavy rainfall," *Journal of Atmospheric and Oceanic Technology*, vol. 30, no. 9, pp. 2063–2080, 2013.

[53] D. Atlas, R. C. Srivastava, and R. S. Sekhon, "Doppler radar characteristics of precipitation at vertical incidence," *Reviews of Geophysics*, vol. 11, no. 1, pp. 1–35, 1973.

[54] G. Wang, R. Zhou, S. Zhaxi, and S. Liu, "Raindrop size distribution measurements on the southeast Tibetan Plateau during the STEP project," *Atmospheric Research*, vol. 249, no. 2, pp. 105311-105312, 2021.

[55] A. Tokay, P. G. Bashor, E. Habib, and T. Kasparis, "Raindrop size distribution measurements in tropical cyclones," *Monthly Weather Review*, vol. 136, no. 5, pp. 1669–1685, 2008.

[56] B. K. Seela, J. Janapati, P.-L. Lin, K. K. Reddy, R. Shirooka, and P. K. Wang, "A comparison study of summer season raindrop size distribution between Palau and Taiwan, two islands in western Pacific," *Journal of Geophysical Research: Atmospheres*, vol. 122, no. 21, pp. 11787–11805, 2017.

[57] J. Janapati, B. K. Seela, P.-L. Lin et al., "Raindrop size distribution characteristics of Indian and Pacific Ocean tropical cyclones observed at India and Taiwan sites," *Journal of the Meteorological Society of Japan*, vol. 98, no. 2, pp. 299–317, 2020.

[58] U. M. Krishna, K. K. Reddy, B. K. Seela, R. Shirooka, P.-L. Lin, and C.-J. Pan, "Raindrop size distribution of easterly and westerly monsoon precipitation observed over Palau Islands in the Western Pacific Ocean," *Atmospheric Research*, vol. 174-175, no. 6, pp. 41–51, 2016.

[59] R. A. Fulton, J. P. Breidenbach, D. J. Seo, D. A. Miller, and T. O' Bannon, "The WSR-88D rainfall algorithm," *Weather and Forecasting*, vol. 13, no. 2, pp. 377–395, 1998.

[60] J. S. Marshall and W. M. K. Palmer, "The distribution of raindrops with size," *Journal of Meteorology*, vol. 5, no. 4, pp. 165-166, 1948.

[61] T. Narayana Rao, B. Radhakrishna, K. Nakamura, and N. Prabhakara Rao, "Differences in raindrop size distribution from southwest monsoon to northeast monsoon at Gadanki," *Quarterly Journal of the Royal Meteorological Society*, vol. 135, no. 643, pp. 1630–1637, 2009.

[62] M. P. Ibañez, A. Pura, R. Sajulga, and S. David, "Raindrop size distribution (RSD) characteristics during the southwest monsoon period in western Luzon, Philippines," *Philippine Journal of Science*, vol. 152, no. S1, pp. 1–16, 2023.